IEEE Access
Multidisciplinary | Rapid Review | Open Access Journal

Received September 23, 2021, accepted October 17, 2021, date of publication October 27, 2021,
date of current version November 30, 2021.

Digital Object Identifier 10.1109/ACCESS.2021.3123742

Force and Velocity Ripple Reduction of the New Linear Motor

MEILING TANG[1,2], YU ZOU[3], SHENGXIAN ZHUANG[1], AND KA WAI ERIC CHENG[3], (Fellow, IEEE)

[1]School of Electrical Engineering, Southwest Jiaotong University, Chengdu, Sichuan 610031, China
[2]Hangzhou Wanxiang Polytechnic, Huangzhou, Zhejiang 310023, China
[3]Electrical Engineering Department, The Hong Kong Polytechnic University, Hong Kong, China

Corresponding author: Meiling Tang (807293429@qq.com)

This work was supported in part by the Excellent Teacher Cultivation Program of Hangzhou High Education System under Project 2019[8], in part by the Hangzhou Philosophy and Social Science Research Base Project through New Rural STEAM Education Research Base under Grant wx2020001, in part by the National Natural Science Foundation of China under Grant U1913214, and in part by the International Cooperation Program of Shenzhen Government under Grant GJHZ20200731095801004.

ABSTRACT This study presents a new linear motor with an E-core stator and a homopolar permanent magnet (PM) mover. The velocity and force ripples of the motor are effectively reduced by an optimized structure and effective force compensation. Firstly, the mechanical structure, magnetic paths and operation principles are introduced. Force analysis is carried out via magnetic circuit method and finite element method (FEM). The magnetic structure of the motor is optimized to reduce the cogging force. Secondly, a force compensation approach is developed to control the velocity and reduce the force ripples of the motor. Parameter identification is employed for the force control to observe the force of the motor so as to compensate the force ripples. Finally, the velocity ripples and force ripples are calculated and measured by simulation and experimentation. Both the simulation and experimental results show high feasibility of the force compensation method. By optimizing the magnetic structure of the motor and developing the force compensation block of the control part, the estimated force output suggests that the force ripples of the motor can be limited within 5%.

INDEX TERMS Cogging force, force ripples, force control, fem, linear motor.

I. INTRODUCTION

Linear motor is a key component in industrial instruments, transportation systems and household appliances, such as position tracking for DNA analysis, rail transportation, linear motor based lifts and linear compressors, etc. [1]–[6]. Traditionally, a rotary motor combined with a linear lead screw rod is usually employed to realize the linear movement. This approach has drawbacks of low positioning accuracy, mechanical backlash, frequent maintenances and calibration, and large spatial volume with a heavy mass. Nowadays, many applications employ direct-drive linear motors to pursuit high accurate control. Direct-drive linear motors can be simply classified as alternative current (AC) linear motor and direct current (DC) linear motor. Some DC linear motors have a short operation stroke. Some of them oscillate with a constant frequency driving operation [7]–[9]. Also, variable frequencies are necessary for some linear oscillating motors (LOMs) [10]–[12]. Regarding the mechanical structures of these motors, their movers could be comprised by coils, permanent magnets (PMs) or iron blocks [13]–[15]. Linear voice coil motors are also popular in the market and widely employed in industrial devices such as wire bonders. They have a fast response and can achieve a high frequency moving cycle due to the light weight of their moving parts. Thus, a rapid acceleration or deceleration can be realized. However, the moving coil must be connected by a wire for power supplying. If the moving part is made of heavy iron, the thrust density of the motor could be relatively low. Some of them are designed and studied as linear compressors for refrigerators [16]. If the moving part is made of PM, the power density of the motor could be improved and the motor can be easily cool down with lump windings embraced in the stator [17]. Halbach PM array has been employed and investigated for LOMs and the efficiency of the LOM can achieve 92 % [18], [19]. However, the stroke length of the

The associate editor coordinating the review of this manuscript and approving it for publication was Zhuang Xu.

mover could be limited to the width of one PM pole due to the mechanical structure of the motor. In [20], the magnetization pattern influence has been analyzed. The results demonstrate that the segment magnets have full performance compared with a magnetic ring. Active magnetic bearings are employed by the LOM to modify the performance [21]. LOMs can be not only used by linear compressors but also employed in many special applications. For instance, artificial heart can employ the miniature LOM to generate mechanical vibrations because the motor occupies a small volume [22]. In [23], the LOM has been employed by a liquid hydrogen pump. In recent years, a lot of industrial equipment require micro components and LOM are employed to realize force control such as microchip surface mounted applications.

In order to realize highly accurate control for linear motors, some advanced control methods have been developed. Force ripple reduction control for linear motors is of high importance for their wide spread employment in the future and this is a hot research topic in recent years [24]. The force ripple to the iron core based linear motors mainly consists of cogging force caused by the reluctance of the salience structure, and the force ripples caused by the variations of motor constant. Also, local magnetic saturation of the motor can deteriorate the force performance. Some optimized mechanical structures are developed to compensate the cogging force of the motor, including the selection of appropriate PM arrangement or materials [25]. Adding additional assistant poles, windings and springs on the mover is an effective way to reduce the cogging force. The screwed structure both on the steel poles and PM poles can also alleviate the cogging force [26]–[30]. Magnetic springs are also investigated for free-piston compressor, energy harvesters and vibration actuator [31]–[33]. Although using magnetic springs could reduce drive losses for linear motors, the nonlinear force output characteristic of magnetic springs could deteriorates the performance of highly precise force control. Apart from the optimization of the mechanical structure, some advanced control methods are developed to mitigate the force ripples of the linear motors [34], [35]. Building accurate force ripple models play a key role to control the force output of the motor. Some force ripple compensators are developed to reduce the force ripples of the motor for the whole stroke length [36]. There are only a few force ripple reduction methods are designed or employed for LOMs until present [37], [38]. In this paper, A tubular PM motor with an E-core stator excited by direct current (DC) power source is introduced. In addition, an adaptive force control is designed and applied for the motor.

In this study, a new magnetic structure of a linear motor with a homopolar PM ring is introduced. Force ripples of the motor have been effectively reduced by both the optimization of mechanical structure especially in the pole optimization. The force ripple identification method is also developed to further mitigate the force ripples during the whole stroke. With the pole optimization and the force compensation, the force ripples can be effectively curbed by identifying and operating on the varied parameters of the motor.

II. MECHANICAL STRUCTURE AND BASIC MODEL

A. MECHANICAL STRUCTURE

This motor mainly consists of the E-core stator, the mover with a surface mounted PM ring and a linear guide, as shown in Figure 1. The E-core stator is embedded into an iron crust which is connected with the interior stator. There is an air gap between the E-core stator and the interior stator. The E-core and the interior stator are made of iron composite and the winding is embraced by the exterior stator. The PM ring is fixed onto the mover which is made of a carbon fiber tube. This configuration has a longer moving distance when compared with other E-core linear motors, since only a small PM ring is employed by the motor. The E-core stator embraces two coils and the coils can be connected in series or parallel.

The mover is guided by a linear guide. A linear encoder is fixed on the basement of the motor to feedback the position of the mover. The three-dimensional (3D) magnetic path and 3D flux distribution generated by the PM is shown in Figure 2. Main flux lines path follow the E-core stator and the interior stator, which suggest that they provide the main magnetic circuit path for the motor. The half cross-sectional schematic of the proposed structure is given in Figure 3. The major specifications of the motor are listed in Table 1.

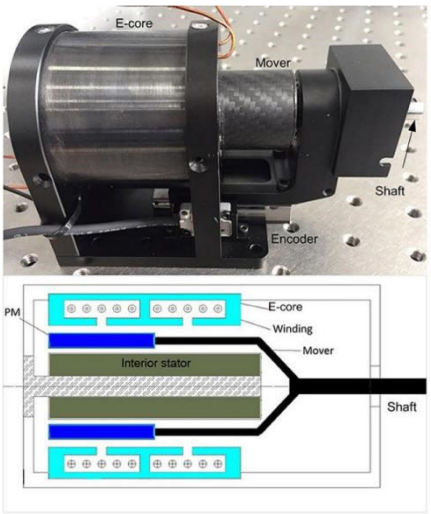

FIGURE 1. Section view of the mechanical structure.

B. MATHEMATIC MODEL

The electric voltage equation and the dynamic equation reflecting the motion characteristics of the motor can be expressed as

$$V = Ri + L\frac{di}{dt} + k\frac{dx}{dt} \tag{1}$$

$$F = M\frac{d^2x}{dt^2} + B\frac{dx}{dt} + Cx + F_l \tag{2}$$

where V is the terminal voltage of the motor and $k\frac{dx}{dt}$ is the back electromotive force (EMF). i, R and L are winding

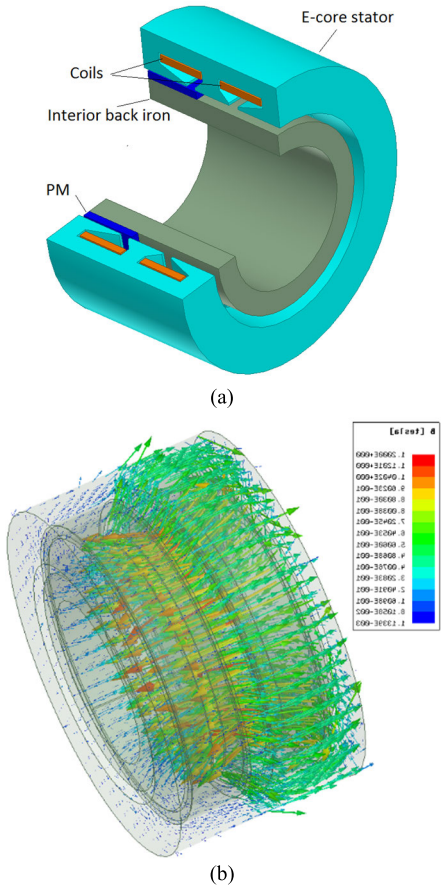

FIGURE 2. (a) The main electric and magnetic part of the motor and (b) 3D FEM simulation to flux distribution.

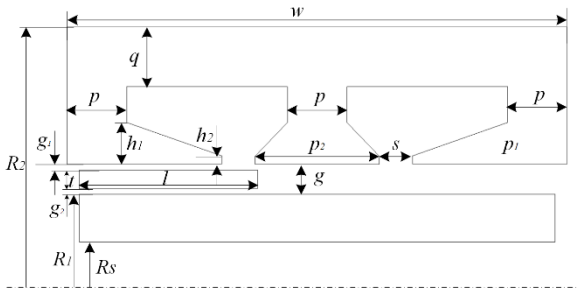

FIGURE 3. The half section scheme of the main structure.

current, resistance and inductance, respectively. x is the displacement of the mover. k is the constant of the motor. M is the mass of the mover. B is the damping coefficient of the motor. C is a coefficient relevant to the displacement of the mover. In this study, it can be regarded as a cogging force factor. F_l denotes the load force to the motor. The electromagnetic force of the motor can be expressed as

$$F = ki \tag{3}$$

According to the equations of the motor, the equivalent model of the motor is shown in Figure 4.

TABLE 1. Main specifications of the motor.

Symbol	Quantity
Rated power (P)	150 W
Rated current of the motor (I)	2 .5 A
Force constant of the motor (k)	25
Diameter of motor (D)	80 mm
Radius of mover (R_2)	26 mm
Stroke length of mover	25 mm
Length of the PM (l)	14 mm
Length of E-core stator (w)	42 mm
Height of the tooth (h_1)	3 mm
Thickness of the PM	3mm
Thickness of the stator yoke(q)	5 mm
Pole width of the stator (p)	5 mm
Mass of mover (M)	69.8 g
Length of air gap 1 (g_1)	0.3 mm
Length of air gap 2 (g_2)	0.3 mm
Length of open slot (s)	3 mm
Winding turns (Nc)	250
Linear encoder accuracy	1 μm

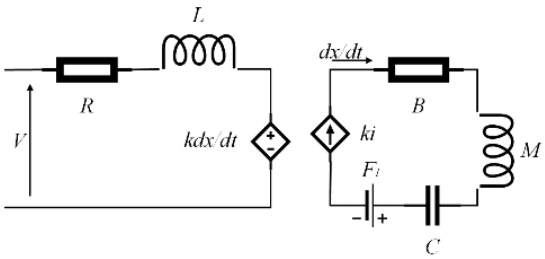

FIGURE 4. The equivalent model of the motor.

C. FORCE ANALYSIS

The mechanical force output of the motor consists of two parts that include the reluctance force and Lorenz force. The reluctance force is mainly produced by the reluctance change of the magnetic circuit path of the motor and the Lorenz force is generated by the current-carrying coils. Also, the cogging force is the reluctance force when the coils are not excited. In order to simplify the study scope, the following assumptions for analyzing the cogging force of the motor are included.

1) Nonlinear characteristics of the iron materials are ignored.
2) The PM ring is magnetized uniformly with identical relative permeability to that of air,
3) Local saturation of magnetic paths is negligible.

The change of the magnetic co-energy W can reflect the reluctance force of the motor according to virtual work principles. When the coils of the motor are not excited, the cogging force of the motor can be calculated by

$$F_m = \frac{dW}{dx} \tag{4}$$

$$W = \frac{1}{2\mu_0}\int_{\Omega} B_g^2 d\Omega \tag{5}$$

where B_g and Ω are the flux density in the air gap and its volume. μ_0 denotes the permeability of the air. Another part of the electromagnetic force is generated by current-carrying coils and this value can be derived by

$$F_a = \int_L idl \times B_s \tag{6}$$

where i is the current in the coil and L is the total length of the coil. B_s denotes the flux density closed by the slot that is fully filled by the coil and this value is generally 1.35 times the value of B_g for the proposed structure. From the basic analysis of the mechanical force output, B_g and B_s play key roles for the force outputs of the motor. Both of them are depended on the magnetic structure of the motor.

In order to calculate the cogging force mentioned before, the flux density in the air gap needs to be obtained when the coils are not excited. The equivalent magnetic circuit is shown as Figure 5 (a) when the mover locates at the left side of the stator. Figure 5 (b) shows the mover at control position.

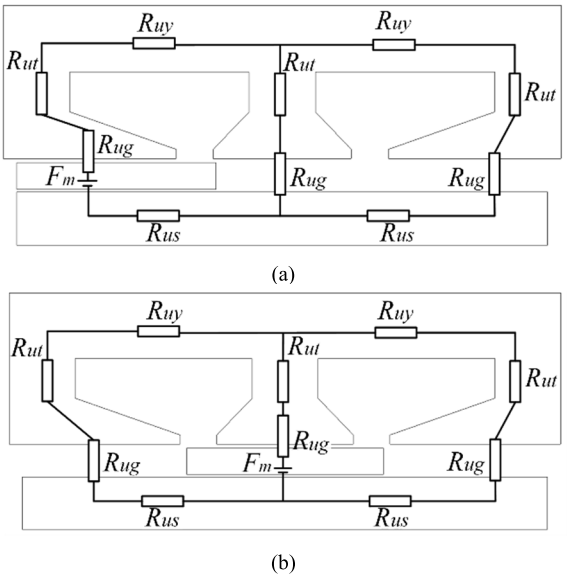

FIGURE 5. The equivalent magnetic circuits of the motor when the mover moves at (a) the left side and (b) the central position.

According to the equivalent magnetic circuits, the reluctances to the Figure 5 (a) and Figure 5 (b) can be calculated.

$$\begin{aligned} R_{\mu 1} &= R_{\mu g} + R_{\mu t} + R_{\mu y} + R_{\mu s} \\ &\quad + \frac{(R_{\mu t} + R_{\mu g}) \cdot (R_{\mu g} + R_{\mu t} + R_{\mu y} + R_{\mu s})}{R_{\mu t} + R_{\mu g} + R_{\mu g} + R_{\mu t} + R_{\mu y} + R_{\mu s}} \end{aligned} \tag{7}$$

$$\begin{aligned} R_{\mu 2} &= R_{\mu g} + R_{\mu t} \\ &\quad + \frac{(R_{\mu g} + R_{\mu t} + R_{\mu y} + R_{\mu s}) \cdot (R_{\mu g} + R_{\mu t} + R_{\mu y} + R_{\mu s})}{R_{\mu g} + R_{\mu t} + R_{\mu y} + R_{\mu s} + R_{\mu g} + R_{\mu t} + R_{\mu y} + R_{\mu s}} \end{aligned} \tag{8}$$

The self-inductance of each coil can be expressed as

$$L = \frac{N^2}{R_\mu} \tag{9}$$

N is the number of turns of the coil and R is the resistance. The flux density in the air gap can be calculated by

$$B_g = \frac{\phi_m}{R_\mu} \tag{10}$$

ϕ_m is the magnetic flux generated by the permanent magnet. Provided that the scalar potential formulation caused by the permanent magnet is defined as $H = -\text{grad}\,\Psi$, the force can be calculated according to equation (5) and be rewritten as equation (11) for finite element method.

$$F_k = \frac{1}{2\mu_0} \sum_{ek} \int_{\Omega_{ek}} [\frac{\partial H}{\partial x} B_g + B_g \frac{\partial H}{\partial x} + B_g^2 |G|^{-1} \frac{\partial |G|}{\partial x}] d\Omega \tag{11}$$

where ek concerns the elements and k is the node of the mesh for calculation. G is the Jacobian matrix, $|G|$ is the determinant of G.

$$G = \begin{vmatrix} \frac{\partial x}{\partial u} & \frac{\partial y}{\partial u} & \frac{\partial z}{\partial u} \\ \frac{\partial x}{\partial v} & \frac{\partial y}{\partial v} & \frac{\partial z}{\partial v} \\ \frac{\partial x}{\partial w} & \frac{\partial x}{\partial w} & \frac{\partial x}{\partial w} \end{vmatrix} \tag{12}$$

where (x, y, z) is the global coordinate and (u, v, w) is the local ones. The flux densities of the motor at different positions are shown in Figure 6.

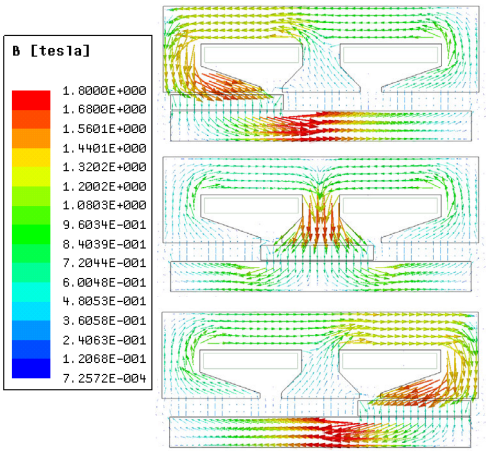

FIGURE 6. The flux density distribution of the motor at different positions.

Apart from the cogging force that can generate force ripples of the motor, local flux saturation can also put negative influence on the force outputs, increasing the total force ripples. It is because that flux saturation would lead to nonlinearity of the reluctance of the equations (7) and (8).This effect is different from that of the cogging force. It can deform the force outputs of the motor during the whole stroke. It can be seen from Figure 6 that the local saturation is severe when the mover locates at the left side or the right side of the stator. The force outputs of the motor could be deformed at these two positions. When the coils are not excited, the force

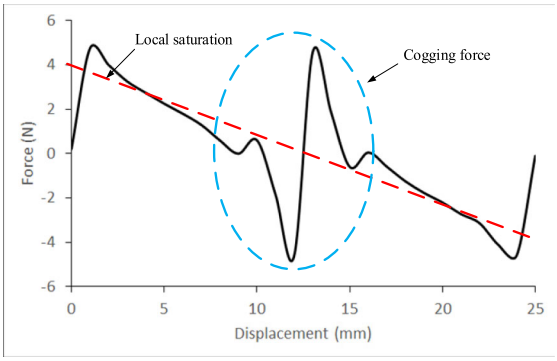

FIGURE 7. Force output deformation of the motor.

outputs of the motor are obtained from FEM results as shown in Figure 7. The deformation of force is mainly caused by two parts. The deformation of force in the stroke is generated by local saturation. The deformed force caused by the ripples during the controlled part of the travel is produced by the cogging force. Both of them are influenced by the excitations of the coils. The maximum of the force is less than 5 N when the motor is not excited.

The cogging force is optimized for the motor, especially for the E-core stator. The optimized parameter include the open slot position, the width of the slot, the PM length and thickness, the tooth shape of the E-core stator. The initial structure of the magnetic path is shown in Figure 8.

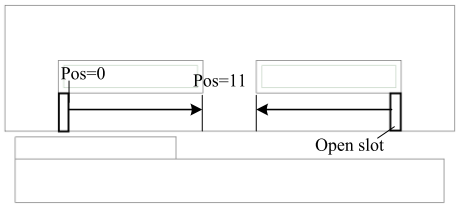

FIGURE 8. The primitive structure of the E-core stator and the moving directions of the open slots when optimizing their positions.

TABLE 2. Main optimized parameters comparison.

Parameters	Initial value	Optimized value
Slot position	6 *mm*	8 *mm*
Slot length	2 *mm*	2.8 *mm*
PM length	20 *mm*	14 *mm*
PM thickness	1.5 *mm*	2 *mm*
Air gap length	2.4 *mm*	2.6 *mm*
Force output	60 *N*	65 *N*
Cogging force	20 *N*	10 *N*

After the optimizations of the magnetic structure, and the resultant magnetic structure is shown in Figure 3. The parameters of the motor before and after the optimization are compared in Table 2. The force outputs of the motor with different excitations are shown in Figure 9 (a). If two coils

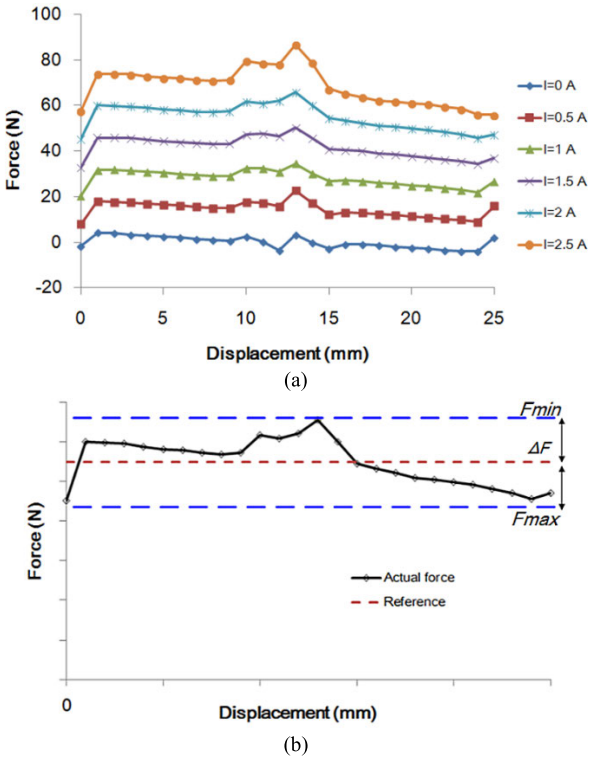

FIGURE 9. (a) Force outputs of the motor under different excitations and (b) the force ripple estimation method for the motor.

are connected in series, it can be seen that the force outputs can reach to70 N when the phase current of the motor is 2.5 A. The force outputs are approximately proportional to the currents. It also shows that the cogging force of the motor increases along with the increase of the phase current. The force ripples caused by the cogging force and local magnetic flux saturation are significantly reduced.

The force ripples of the motor can be defined as the following equation (13) and this equation can be explained by Figure 9 (b). The force ripples can be calculated by the rate of the maximum deviation between the actual force and the reference force provided for the motor.

$$F_{ripple} = \frac{max(F_{max} - F_{ref}, F_{min} - F_{ref})}{F_{ref}} \times 100\% \quad (13)$$

III. FORCE CONTROL

Generally, three-closed-loop control is employed by many servo motors in industry and this control approach is also

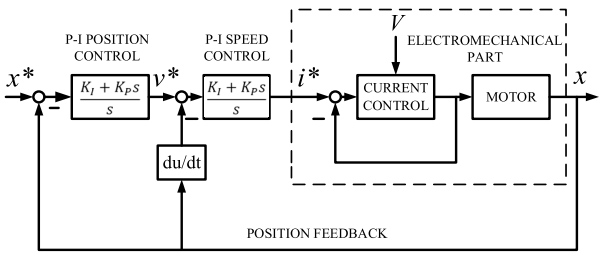

FIGURE 10. The control scheme of the motor.

used for this motor. The whole control scheme is shown in Figure 10. The position controller and the speed controller are proportional-integral (PI) control. The current command is provided by the output of the speed controller. Cascading a current control loop with the motor for the motor current regulation. The position feedback of the motor will be provided for the position controller and the speed controller. The electromechanical part is the main part of the control plant.

According to the mathematic model of the motor from equations (1) and (2), the transfer function from the terminal voltage to the current in coils can be expressed by

$$\frac{i(s)}{V(s)} = \frac{\frac{1}{R}}{\frac{L}{R}s + 1} \tag{14}$$

If the current loop gain is k_c for a current converter to the motor coils and a PI controller is employed for the inner current loop, the closed-loop transfer function of the current loop can be

$$\frac{i(s)}{i^*(s)} = \frac{k_c(k_p s + k_i)}{Ls^2 + \left(R + k_c k_p\right)s + k_c k_i} \tag{15}$$

As $k_c k_p \gg R$, the resistance can be negligible. The transfer function can be rewritten as

$$\frac{i(s)}{i^*(s)} = \frac{\frac{k_c k_p s}{L} + \frac{k_c k_i}{L}}{s^2 + \left(\frac{k_c k_p}{L}\right)s + \frac{k_c k_i}{L}} \tag{16}$$

The parameters of the PI controller can be determined by the damping factor ξ and the natural frequency ω_n.

$$k_p = \frac{2\xi\omega_n L}{k_c} \tag{17}$$

$$k_i = \frac{\omega_n^2 L}{k_c} \tag{18}$$

Equation (3) shows the relationship between the electromagnetic force and the current by the motor constant k. Therefore, the transfer function from current to the position of the mover is

$$\frac{x(s)}{i(s)} = \frac{k}{Ms^2 + Bs + C} \tag{19}$$

The force control for the electromechanical part of the motor is shown in Figure 11. This control part mainly consists of three closed loops including the current loop, the back-EMF loop, and the force loop. All the loops are under feedback control to regulate the current of motor coils. From the force analysis mentioned before, force output deformation of the motor is mainly caused by the local magnetic saturation and the cogging force. Force output with respect to phase current becomes nonlinear if local magnetic saturation occurs. Also, the back-EMF could be nonlinear to the speed of the motor as the motor constant cannot remain unchanged during the whole stroke and operation conditions. The force observer and the cogging force are used to compensate for the current control loop of the motor, as shown in Figure 12. The force compensation block addresses the nonlinear characteristics

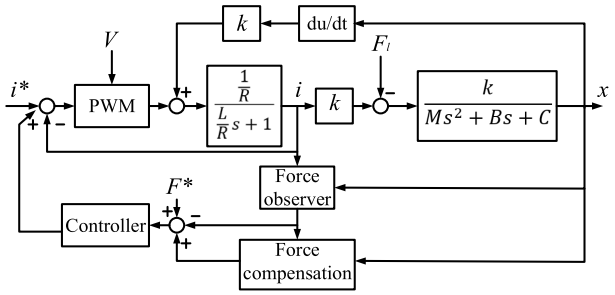

FIGURE 11. The force control of the electromechanical part.

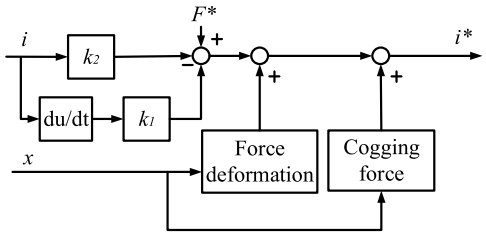

FIGURE 12. The force compensation block for the motor.

of the motor constant k, which is a function of position and the current. This block is fed back to regulate the current by combining with the nonlinear motor constant k, the cogging force and the force load to the motor.

The force load is equivalent to a constant and is proportional to the coil current. The cogging force and large force output deformation can be estimated by FEM, and are compensated by the force control part. The nonlinear factors to the motor including the nonlinear motor constant and tiny noises to current sampling signals and other disturbances can be taken as a factor that is proportional to the rate of change of the current when the motor is operated in a steady state. Therefore, equation (19) can be rewritten as

$$\frac{x(s)}{i^*(s)} = \frac{k_1 s + k_2}{Ms^2 + Bs + C} \tag{20}$$

k_1 is relatively small as it represents the influence of the tiny disturbances to the current and k_2 is a constant reflecting the total force output of the mover which is directly influenced by the current. To obtain k_1 and k_2, physically measuring the force output by using a force sensor and a manual position adjustment. In addition, a carriage to fix the mover of the motor and a frictionless air bearing support for precise measurement is necessary. Therefore, it is difficult to precisely measure the force output and the force-deformation of the motor. The reference force output of the motor can be obtained according to the theoretical analysis in the mathematical model part. The force ripples and force deformations can be determined in this way. If the structure of the motor and necessary parameters of the motor are given, the magnetic field distribution can be obtained by FEM, and electromagnetic forces can be calculated precisely at each position when the motor is excited. Although FEM can estimate the forces, the errors between the analytical design and actual application always exist. In order to solve

this problem, combining the FEM results with parameters identification approach is an effective solution for accurate control of the motor. The basic force features can be estimated by FEM such as cogging force and deformation caused by local saturation. Then, the estimated error will be regarded as a disturbance to the parameters identification of the motor. According to equation (20), the motor constant can be identified by the following equations. Taking the current input i and the mover displacement x as the inputs of the identification system, equation (20) can be rewritten as a discrete-time form

$$A\left(z^{-1}\right)x\left(t\right) = B\left(z^{-1}\right)i\left(t\right) + \varepsilon\left(t\right) \tag{21}$$

$\varepsilon(t)$ is regarded as a disturbance caused by the estimated error and external disturbances to the control system.

$$A\left(z^{-1}\right) = 1 + a_1 z^{-1} + a_2 z^{-2} \tag{22}$$

$$B\left(z^{-1}\right) = b_0 + b_1 z^{-1} \tag{23}$$

If a_1, a_2, b_0 and b_1 can be identified and the mass of the mover, damping coefficient B and coefficient C are estimated, the motor constant can be obtained even though the motor owns some nonlinear characteristics. These parameters can be identified according to the least-square matrix form as shown in equation (24).

$$\boldsymbol{x}\left(t\right) = \boldsymbol{\varphi}^T\left(t-1\right)\boldsymbol{\theta}\left(t-1\right) + \boldsymbol{\epsilon}\left(t\right) \tag{24}$$

$$\begin{cases} \boldsymbol{\theta} = [a_1, a_2, b_0, b_1] \\ \boldsymbol{\varphi}^T\left(t-1\right) = [-x\left(t-1\right), -x\left(t-2\right), i\left(t-1\right), i(t-2)] \end{cases} \tag{25}$$

$\boldsymbol{\epsilon}(t)$ is the residual. $\boldsymbol{\theta}$ can be identified by recursive least square algorithm with the forgetting factor ρ according to the following steps.

$$\hat{\boldsymbol{\theta}}\left(t\right) = \hat{\boldsymbol{\theta}}\left(t-1\right) + \boldsymbol{G}(t)\cdot\left(x\left(t\right) - \boldsymbol{\varphi}^T\left(t\right)\hat{\boldsymbol{\theta}}\left(t-1\right)\right) \tag{26}$$

$$\boldsymbol{G}\left(t\right) = \frac{\boldsymbol{P}\left(t-1\right)\boldsymbol{\varphi}^T\left(t\right)}{\left(\rho + \boldsymbol{\varphi}^T\left(t\right)\boldsymbol{P}(t-1)\boldsymbol{\varphi}(t)\right)^{-1}} \tag{27}$$

$$\boldsymbol{P}\left(t\right) = \left(I - \boldsymbol{G}\left(t\right)\boldsymbol{\varphi}^T\left(t\right)\right)\cdot\frac{\boldsymbol{P}\left(t-1\right)}{\rho} \tag{28}$$

$\boldsymbol{P}(t)$ and $\boldsymbol{G}(t)$ are the covariance matrix and the adjusting gain. ρ is usually chosen between 0.95∼1 for this motor. $\boldsymbol{P}(t)$ should be a matrix with limited scope of values for each element at the initial time. I is a unit matrix. The convergence of the iterative algorithm had been proved in [39]. If the following conditions are satisfied, the system is stable.

1) The measurement vector sequence $\boldsymbol{\varphi}(t)$ is persistently exciting, and $\lim_{t\to\infty}\frac{1}{t}\sum_{j=1}^{t}\boldsymbol{\varphi}(j)\boldsymbol{\varphi}^T(j)$ exists;
2) The vector $\boldsymbol{\epsilon}(t)$ is an independent random variable with zero mean;
3) The parameter change rate $\boldsymbol{\alpha}\left(t\right) = \boldsymbol{\theta}\left(t\right) - \boldsymbol{\theta}\left(t-1\right)$ is bounded, $\boldsymbol{\alpha}(t)$ and $\boldsymbol{\epsilon}(t)$ are independent,

$$E\left\|\boldsymbol{\alpha}\left(t\right)\right\|^2 < \infty \tag{29}$$

$$E\left[\boldsymbol{\alpha}\left(t\right)\boldsymbol{\epsilon}\left(t\right)\right] = 0 \tag{30}$$

as $t \to \infty$, the parameters $\boldsymbol{\theta}(t)$ will be bounded and they are identifiable by recursive least square method with forgetting factor. Under the designed control method, the system is stable if the system inputs and outputs are bounded.

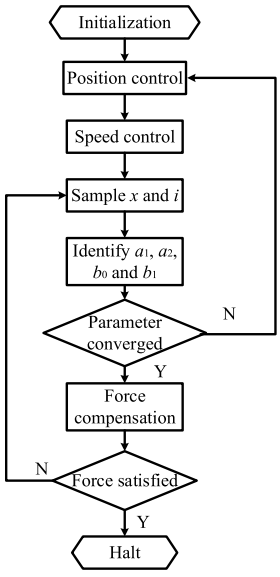

FIGURE 13. The force compensation flow chart for the motor.

The machine halt rule should obey equation (31).

$$\frac{\hat{\boldsymbol{\theta}}\left(t\right) - \hat{\boldsymbol{\theta}}\left(t-1\right)}{\hat{\boldsymbol{\theta}}\left(t\right)} < e \tag{31}$$

where e is a small positive number. The whole force compensation algorithm can be plotted as Figure 13.

When the motor is operated in the position and speed control, the positions and current are sampled digitally. Then, parameter identification is carried out to get the parameters of the control subject. The force compensation works if identified parameters are converged. The force control finished if the force ripples are fulfill the requirements to practical application.

IV. SIMULATION RESULTS

A multi-physical domain simulation block is built according to the theoretical analysis, as shown in Figure 14. This block consists of the control part, the FEM part, the electric part and the mechanical part. The control part includes the controller and the force compensation, and the FEM part is the designed magnetic structure with coils via an FEM software package. The electric components involve a resistor reprinting the resistance of the winding and an inductor denoting the armature inductance of the motor. The current can be controlled after obtaining the signal from the controller. The mechanical part mainly has a damper and a mass cube box, and their parameters are given according to the practical values of the motor. By transient simulation of an FEM software (e.g. ANSYS), the position and velocity of the mover can be obtained at each simulation step if the mass of the mover and damping factor of the motor are assigned. The control part

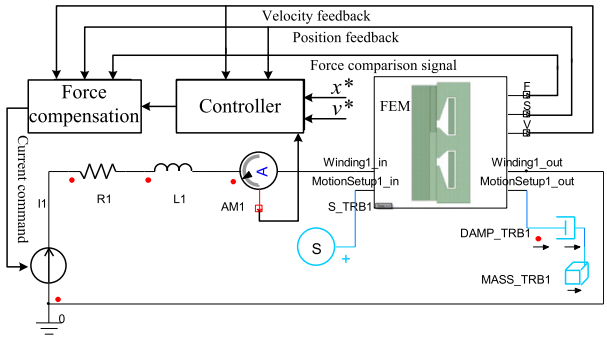

FIGURE 14. The simulation block of the motor control.

and the electric part can be built in software ANSYS Simplorer. Two software packages can realize the data interaction timely through each other. Position and velocity signals are calculated by the FEM part and then these signals are used for the force compensation. The force compensation obtains the phase current through an ampere meter and outputs the signal to the controller. The controller will supply the control signal to govern a current source for the motor.

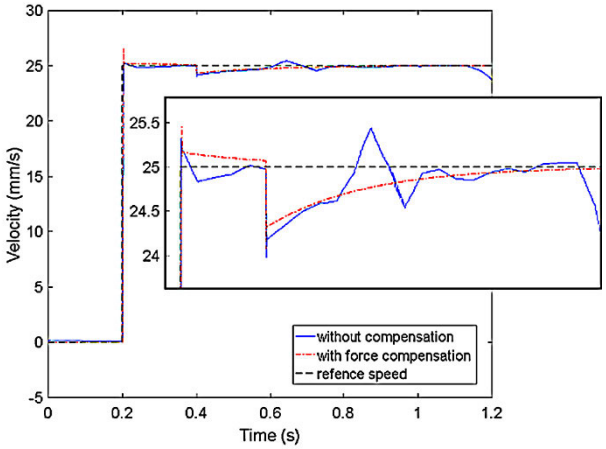

FIGURE 15. Velocity of the mover in the comparison of the controller with and without force compensation.

The velocity of the motor is obtained by the simulation model, as shown in Figure 15. A step velocity reference is supplied to the controller for the motor. The reference increases from zero to 25 mm/s at 0.2 s. A force load 10 N is added on the motor at the time of 0.4 s. The velocity responses under different controllers are obtained and the velocity ripples are plotted in the Figure 15. The velocity increases to 25 mm/s quickly and decreases to 24 mm/s when the load force is applied to the mover. Then, the velocity gradually approaches to the reference velocity. Force ripples vibrate obviously if the motor is controlled without force compensation. The velocity response governed by the controller with the force compensation is smooth and the performance of the linear motor becomes obviously better than that without the force compensation.

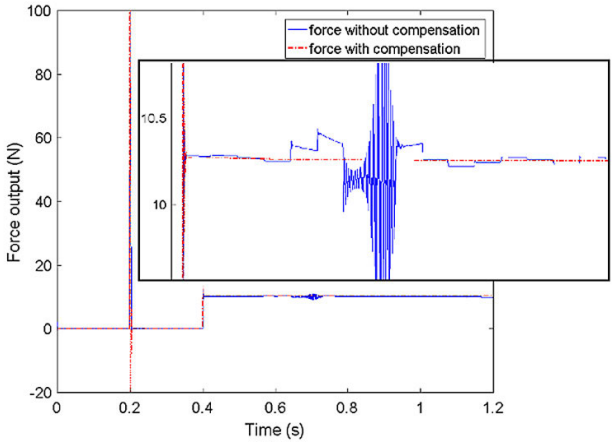

FIGURE 16. The force outputs of the motor with different controllers.

With the same reference, the force response of the motor is obtained as shown in Figure 16. The force response is slightly larger than the force load. From the figure, the force output vibrates dramatically when the mover approaches the middle tooth of the E-core stator. This vibration and force ripples are eliminated if the force compensation is provided for the controller and the force output almost remains constant from the simulation result.

V. EXPERIMENTAL VERIFICATION

A. EXPERIMENTAL SETUP

The prototype is manufactured and an experimental setup is built to test the designed motor, as shown in Figure 17. The whole experimental components include the liner motor, a force gauge to test the force of the motor, a power supplier, a voltage controlled current driver and a dSPACE card DS1104 embedded in a personal computer. The power supplier provides the voltage to the current driver whose current output is controlled by the DS1104 via the with a digital to analogue (DAC) port. The position of the linear motor is sampled by a linear encoder (RENISHAW, revolution 1μm) and this signal is fed back to the DS1104 card according to an encoder interface. The force gauge can output the measured value to the computer also. The force gauge and

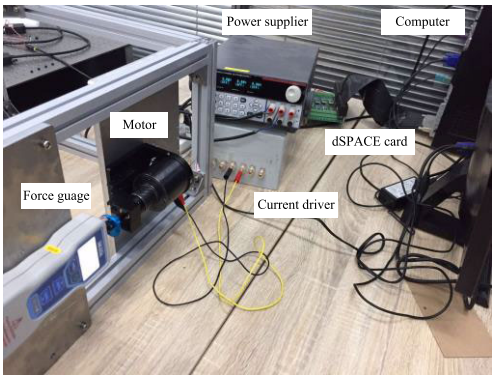

FIGURE 17. Experimental setup.

the motor are fixed on a mechanical support. After obtaining the signals from the linear encoder and the force gauge, the DS1104 can be regarded as controller for the current driver and the program debugged to the card has been built by the software package of MATLAB/Simulink. The entire control scheme is developed by Simulink blocks that are similar to the simulation blocks so that the control algorithm is identical to the theoretical analysis. The sampling time for the whole control system is selected as 0.001s.

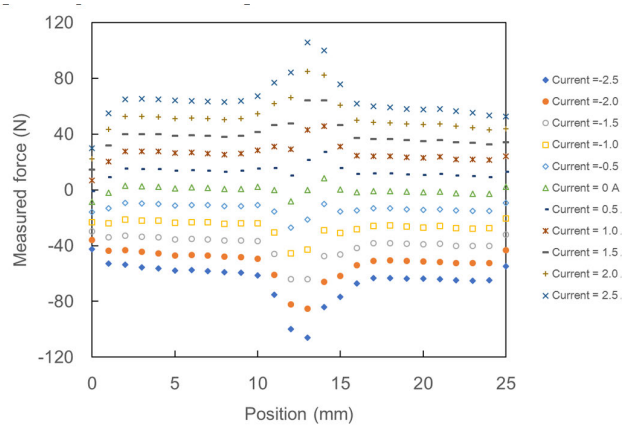

FIGURE 18. Force measurement when the winding is excited with different current excitations.

TABLE 3. Force output in comparison with other linear motors.

Motor Type	Force to Mover Weight (N/Kg)	Force to PM Weight (N/Kg)
CBD	24	120
T-M-IP	15	150
T-C-M-IP	16	170
T-M-SI	17	150
U-core	25	170
Proposed LOM	30	200

B. FORCE MEASUREMENT

Measured force outputs are shown in Figure 18 when the mover is located at different positions from zero to 25 mm. Two coils are connected in series with an identical current direction. It can be seen that the force output profiles are nearly symmetrical to the current direction of the winding. When the current increases from zero to 2.5 A with the interval of 0.5 A, the force outputs are nearly proportional to current values, increasing from zero to average of 70 N. Interestingly, the force outputs become negative if the current direction reverses. The force values are symmetrical to the force curve with zero winding currents. The cogging force ripples are mainly concentrated at the central tooth of the stator. The mover weight of the proposed motor is 1 *kg* and the PM weight of the motor is 150 *g*. The force output ratio to the mover weight and PM weight is compared with other types of linear motors given in the paper [40] and the proposed motor performances better than other type linear motors, as shown in Table 3. In addition, if the stator is replaced by an U core with one coil, the force density will be reduced and a long-stroke movement is hard to achieve in the practical situation. Figure 19 shows the core loss of the motor operating at different frequencies.

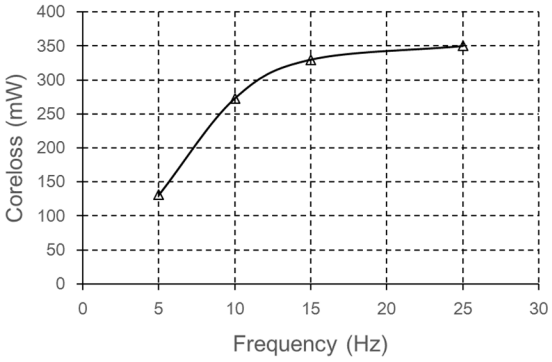

FIGURE 19. Core-loss of the motor when mover moves at different moving frequencies.

C. FORCE AND VELOCITY CONTROL

The cogging force ripples are mainly concentrated at the central part of the toothed stator. A step velocity reference is provided for the motor and the responses of velocity are shown in Figure 20 (a). The reference is 25 mm/s and the motor is operated within 0.6 s. The motor operates with no mechanical load and the velocity can reach the reference

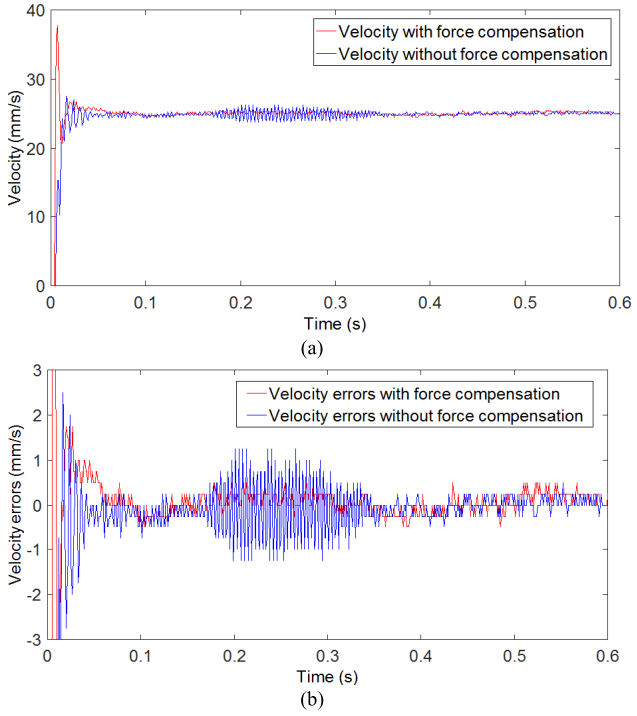

FIGURE 20. (a) Velocity responses with no force load (b) velocity errors of the motor.

value within 0.05 s. The velocity response is compared with the result governed by the controller combing force compensation. There are some velocity vibrations at the middle part if the force compensation is not applied in the control, though both velocities can reach the reference value provided. The vibration amplitude exceeds 1 mm/s, as shown in Figure 20 (b). These vibrations are mainly caused by the force vibration and they can be effectively alleviated by adding the force compensation for the control part of the motor.

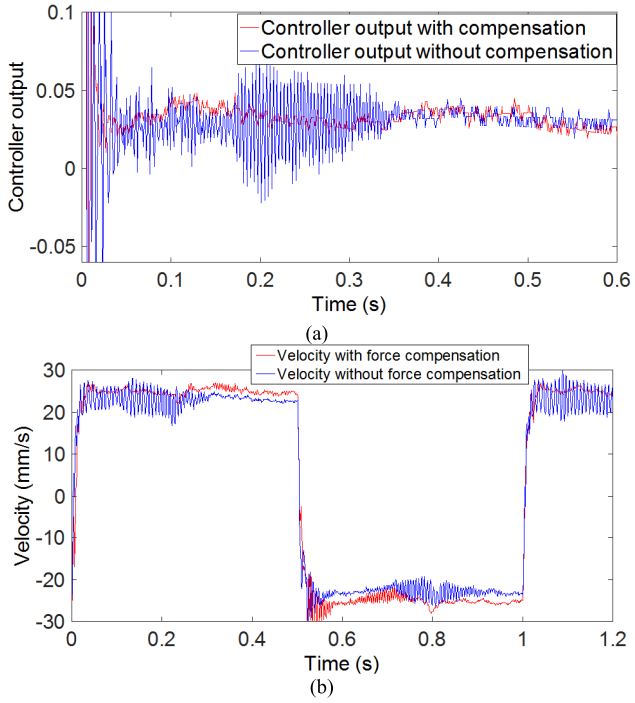

FIGURE 21. (a) The controller output when the motor is operated with no force load and (b) Velocity responses of the motor with a load.

The outputs of the controller for the motor are given in Figure 21 (a). It can be seen the output of the controller is also influenced by the velocity ripples as the velocity is a feedback to the controller. The output should be regulated according to the velocity error. The vibration of the output from the controller combing force compensation is extensively smaller than that without force compensation. It suggests that the force compensation can curb the velocity vibration effectively. According to the simulations, the velocity vibration could be a result of force vibration generated by cogging force and other force disturbances to the motor.

When the motor is operated with a periodical square wave reference and a varied load is added on the motor by connecting the mover to a spring fixed on the experimental platform, the velocity responses are obtained as shown in Figure 21 (b). The amplitude of the reference is 25 mm/s and the frequency is 1 Hz. if a controller without force compensation regulates the velocity of the motor, the velocity profile will produce obvious vibrate and a steady state error exists during the entire stroke. The velocity cannot achieve the reference value after

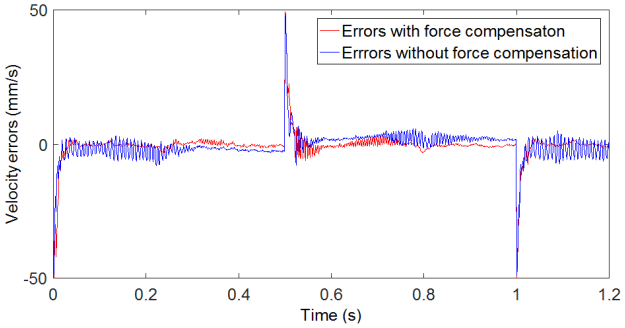

FIGURE 22. Velocity errors of the motor with force load.

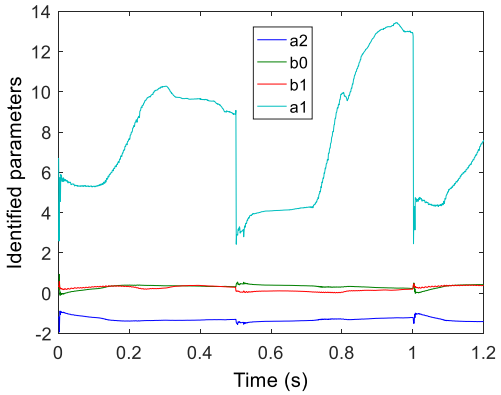

FIGURE 23. Identified parameters of the motor with varied force loads.

the velocity profile is stable and the steady state error is up to 3 mm/s, as shown in Figure 22. The maximum vibration exceeds 7 mm/s. Obviously, the large vibration of the speed can be eliminated if the force compensation is applied in the control system. Also, the velocity response can reach the reference value of 25 mm/s and the steady error is 1 mm/s. Apart from the vibration alleviation, the steady state error of the motor velocity can be also reduced by adding force compensation. The force compensation block can compensate the force ripples according to the identified parameter shown in Figure 23. These parameters not only reflect the parameters of the motor but also the dynamic parameter variation of the whole motion system. The parameter *a1* changes dramatically compared with other parameters because this parameter is a coefficient of the acceleration of the mover.

The force output can be estimated as shown in Figure 24 when the motor is controlled with a load of 10 N. By comparing the estimated force outputs with different controllers, the performance of the motor with force compensation shows that fewer force ripples can be realized by the proposed control approach. If the force output is 10 N, the force ripple is ± 1.5 N while using the controller without the force compensation. After employing the force compensation block, the controller of the motor can limit the force ripple to ± 0.5 N. Therefore, the force ripple of the motor can be controlled within 5%. If the force reference is 10 N and the terminal of the mover reaches the testing tip of the force gauge that is fixed on the mechanical support without any movement,

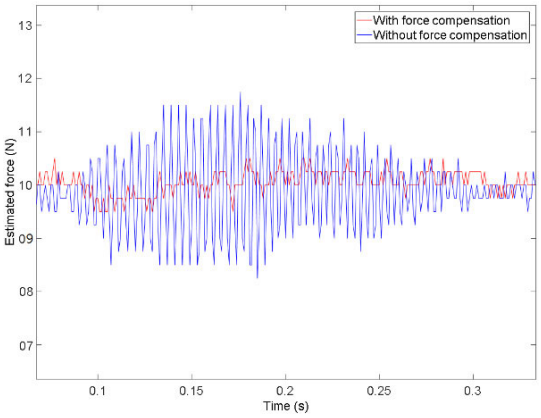

FIGURE 24. Estimated force outputs of the motor with different controllers under a constant force load.

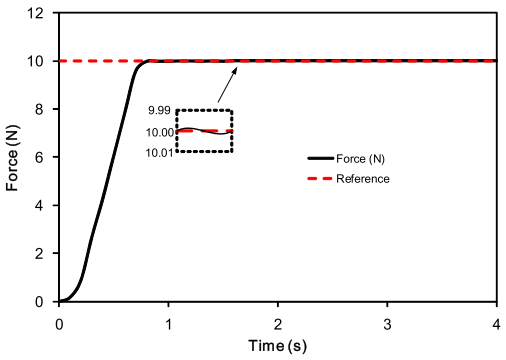

FIGURE 25. The static force control of the motor.

TABLE 4. PI controller parameters.

Symbol	Quantity
Proportional gain of position loop	120
Integral gain of position loop	150
Proportional gain of current loop	2.2
Integral gain of current loop	528.8

the force response is obtained as shown in Figure 25. The static force control error is within ±0.01 N, which is an excellent performance when compared with other existing linear motor products employed in industry.

For the experiment, a spring is fixed at the end of the experimental platform. The spring, as an inconstant load, is also connected with the mover of the motor. If the force output command is 10 *mN* at the position of 10 *mm*, Figure 26 (a) shows the curves measured at the speed of 100 *mm/s* and 250 *mm/s*, respectively. The data sampling interval is 2 *ms* for these curves and corresponding PI controllers' parameters are listed in Table 4. Under the identical force output command at the position of 25 *mm*, the curves are shown in Figure 26 (b).

It can be seen that the force output can be controlled accurately with the proposed force compensation method if

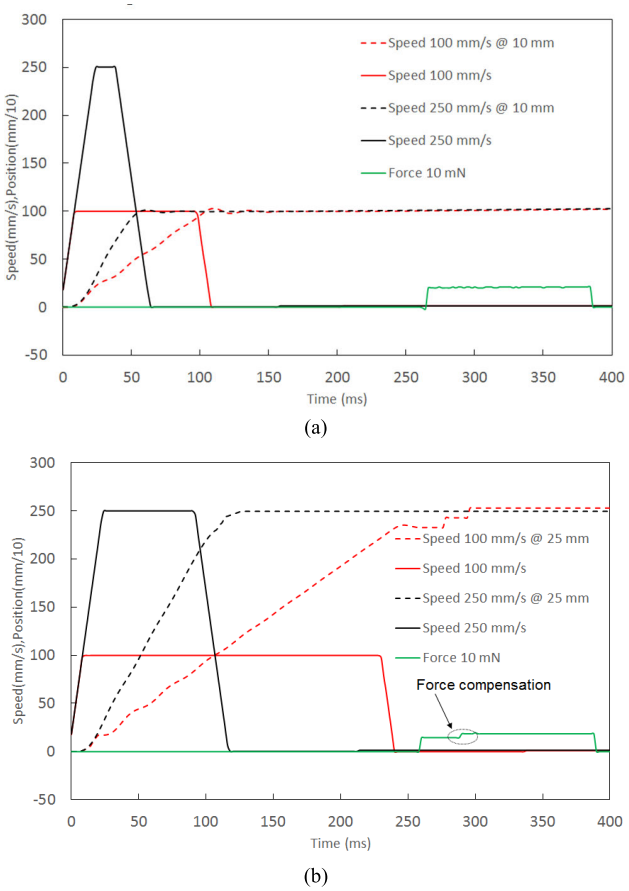

FIGURE 26. Force output measurements with different speed at position (a) 10 mm and (b) 25 mm.

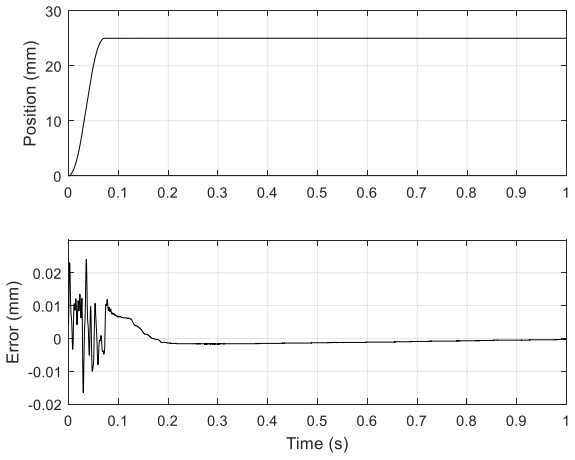

FIGURE 27. Position step response of the motor and position errors obtained by experiments.

a spring load on the mover of the motor. Compared with Figure 26 (a) and (b), the longer the loading spring is, the larger the force compensation imposing on the mover. The position step response is plotted in Figure 27 when the mover moves from original position to the position of 25 *mm*. Position tracking errors are obtained from the experiment. The position error can be reduced to 0.01 *mm* at 0.08 *s*. It takes

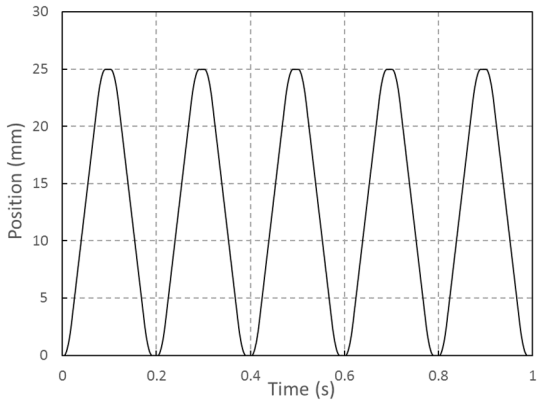

FIGURE 28. Position step response of the motor under an oscillating reference of 5 Hz.

the motor 0.2 s to reach the position of 25 *mm* with the position error less than 0.002 *mm*. Finally, the position error is less than 0.001 *mm* according to the data of Figure 27. When the position error is limited in 0.01 mm, the mover can achieve 5 Hz under the an oscillating position reference, as shown in Figure 28.

VI. CONCLUSION

In this paper, a linear motor equipped with an E-core stator is proposed and the force ripple reduction is realized by optimizing the magnetic path structure of the motor and designing a force compensation method. The structure and operation principles of the motor are firstly introduced. This motor has only one PM ring mounted on the surface of the mover and the moving stroke can be improved by this structure. The force output of the motor has been analyzed by combing magnetic circuit path estimation and FEM. The cogging force and force ripple caused by local flux saturation is also analyzed, followed by the magnetic structure optimization to reduce the cogging force. Finally, a force compensation approach is designed with parameter identification, constructing a force compensation block. Both the simulation and experiments show that the velocity ripples of the motor can be effectively reduced. By estimating the force output, the force ripples of the motor can be limited to 5%. The static force control error can be controlled within the range of ± 0.01 N. These results prove the effectiveness of the designed force ripple reduction. The main contribution of the study can be concluded as follows.

1) A new linear motor structure for short-stroke motion has been proposed and its structure has been optimized to reduce the cogging force.
2) An effective force ripple reduction methodology has been developed through an innovative force compensation method.
3) Parameter identification is employed for the force compensation block and the controller of the motor. The performance of the motor has been improved substantially by reducing the velocity ripples and force output ripples.

ACKNOWEDGEMENT

MeiLing Tang developed the analysis, hardware design and measurement. Yu Zou conducted the simulation of the work. Shengxian Zhuang was responsible for the background theory. Ka Wai Eric Cheng provided the guidance and supervision of the study.

REFERENCES

[1] A. Safa, R. Y. Abdolmalaki, and H. C. Nejad, "Precise position tracking control with an improved transient performance for a linear piezoelectric ceramic motor," *IEEE Trans. Ind. Electron.*, vol. 66, no. 4, pp. 3008–3018, Apr. 2019.
[2] D. Wang, D. Zhang, X. Du, and X. Wang, "Unitized design methodology of linear switched reluctance motor with segmental secondary for long rail propulsion application," *IEEE Trans. Ind. Electron.*, vol. 65, no. 12, pp. 9884–9894, Dec. 2018.
[3] H. Seo, J. Lim, G.-H. Choe, J.-Y. Choi, and J.-H. Jeong, "Algorithm of linear induction motor control for low normal force of magnetic levitation train propulsion system," *IEEE Trans. Magn.*, vol. 54, no. 11, pp. 1–4, Nov. 2018.
[4] H. Fan, K. T. Chau, C. Liu, L. Cao, and T. W. Ching, "Quantitative comparison of novel dual-PM linear motors for ropeless elevator system," *IEEE Trans. Magn.*, vol. 54, no. 11, pp. 1–6, Nov. 2018.
[5] J. Y. Yoon, J. H. Lang, and D. L. Trumper, "Fine-tooth iron-core linear synchronous motor for low acoustic noise applications," *IEEE Trans. Ind. Electron.*, vol. 65, no. 12, pp. 9895–9904, Dec. 2018.
[6] X. Xue, K. W. E. Cheng, and Z. Zhang, "Model, analysis, and application of tubular linear switched reluctance actuator for linear compressors," *IEEE Trans. Ind. Electron.*, vol. 65, no. 12, pp. 9863–9872, Dec. 2018.
[7] I. Boldea, L. Tutelea, W. Xu, and M. Pucci, "Linear electric machines, mrives, and MAGLEVs: An overview," *IEEE Trans. Ind. Electron.*, vol. 65, no. 9, pp. 7504–7515, Sep. 2018.
[8] I. Boldea, *Linear Electric Machiens, Drives and MAGLEVs Handbook*. Boca Raton, FL, USA: CRC Press, 2013.
[9] S. Masoudi, M. R. Feyzi, and M. B. B. Sharifian, "Force ripple and jerk minimisation in double sided linear switched reluctance motor used in elevator application," *IET Electr. Power Appl.*, vol. 10, no. 6, pp. 508–516, Jul. 2016.
[10] D. Wang, X. Du, D. Zhang, and X. Wang, "Design, optimization, and prototyping of segmental-type linear switched-reluctance motor with a toroidally wound mover for vertical propulsion application," *IEEE Trans. Ind. Electron.*, vol. 65, no. 2, pp. 1865–1874, Feb. 2018.
[11] J. G. Amoros, P. Andrada, B. Blanque, and M. Marin-Genesca, "Influence of design parameters in the optimization of linear switched reluctance motor under thermal constraints," *IEEE Trans. Ind. Electron.*, vol. 65, no. 2, pp. 1875–1883, Feb. 2018.
[12] H. Chen, W. Yan, and Z. Li, "Flux characteristics analysis of a single-phase tubular switched reluctance linear launcher," *IEEE Trans. Plasma Sci.*, vol. 47, no. 5, pp. 2316–2322, May 2019.
[13] J. F. Pan, Y. Zou, and G. Cao, "An asymmetric linear switched reluctance motor," *IEEE Trans. Energy Convers.*, vol. 28, no. 2, pp. 444–451, Jun. 2013.
[14] G. Baoming, A. T. D. Almeida, and F. J. T. E. Ferreira, "Design of transverse flux linear switched reluctance motor," *IEEE Trans. Magn.*, vol. 45, no. 1, pp. 113–119, Jan. 2009.
[15] M. Toshiaki and F. Shunsuke, "Design of coil specificaitons in EDS Maglev using an optimization program," in *Proc. Rec. LDIA*, Tokyo, Japan, 1998, pp. 343–346.
[16] S. G. Min and B. Sarlioglu, "3-D performance analysis and multiobjective optimization of coreless-type PM linear synchronous motors," *IEEE Trans. Ind. Electron.*, vol. 65, no. 2, pp. 1855–1864, Feb. 2018.
[17] Y. Zou and K. W. E. Cheng, "Design and optimization of a homopolar permanent-magnet linear tubular motor equipped with the E-core stator," *IEEE Access*, vol. 7, pp. 134514–134524, 2019.
[18] Z. Q. Zhu and X. Chen, "Analysis of an E-core interior permanent magnet linear oscillating actuator," *IEEE Trans. Magn.*, vol. 45, no. 10, pp. 4384–4387, Oct. 2009.
[19] J. Wang, D. Howe, and Z. Lin, "Design optimization of short-stroke single-phase tubular permanent-magnet motor for refrigeration applications," *IEEE Trans. Ind. Electron.*, vol. 57, no. 1, pp. 327–334, Jan. 2010.

[20] S. Wang, J. Kang, M. Degano, A. Galassini, and C. Gerada, "An accurate wide-speed range control method of IPMSM considering resistive voltage drop and magnetic saturation," *IEEE Trans. Ind. Electron.*, vol. 67, no. 4, pp. 2630–2640, Apr. 2020.
[21] H. Karimi, S. Vaez-Zadeh, and F. R. Salmasi, "Combined vector and direct thrust control of linear induction motors with end effect compensation," *IEEE Trans. Energy Convers.*, vol. 31, no. 1, pp. 196–205, Mar. 2016.
[22] D. Xu, B. Wang, G. Zhang, G. Wang, and Y. Yu, "A review of sensorless control methods for AC motor drives," *CES Trans. Elect. Mach. Syst.*, vol. 2, no. 1, pp. 104–115, Mar. 2018.
[23] M. Abdelrahem, C. M. Hackl, and R. Kennel, "Finite position set-phase locked loop for sensorless control of direct-driven permanent-magnet synchronous generators," *IEEE Trans. Power Electron.*, vol. 33, no. 4, pp. 3097–3105, Apr. 2018.
[24] M. Seilmeier and B. Piepenbreier, "Sensorless control of PMSM for the whole speed range using two-degree-of-freedom current control and HF test current injection for low-speed range," *IEEE Trans. Power Electron.*, vol. 30, no. 8, pp. 4394–4403, Aug. 2015.
[25] S. W. Zhao, N. C. Cheung, W.-C. Gan, and Z. G. Sun, "A novel flux linkage measurement method for linear switched reluctance motors," *IEEE Trans. Instrum. Meas.*, vol. 58, no. 10, pp. 3569–3575, Oct. 2009.
[26] W. Wei, Q. Wang, and R. Nie, "Sensorless control of double-sided linear switched reluctance motor based on simplified flux linkage method," *CES Trans. Electr. Mach. Syst.*, vol. 1, no. 3, pp. 246–253, Sep. 2017.
[27] I. I. Abdalla, T. Ibrahim, and N. M. Nor, "Analysis of tubular linear motors for different shapes of magnets," *IEEE Access*, vol. 6, pp. 10297–10310, 2018.
[28] J.-S. Shin, R. Watanabe, T. Koseki, and H.-J. Kim, "Practical design approach of a transverse flux linear synchronous motor for compact size, small mover weight, high efficiency, and low material cost," *IEEE Trans. Magn.*, vol. 51, no. 3, pp. 1–4, Mar. 2015.
[29] S. W. Youn, J. J. Lee, H. S. Yoon, and C. S. Koh, "A new cogging-free permanent-magnet linear motor," *IEEE Trans. Magn.*, vol. 44, no. 7, pp. 1785–1790, Jul. 2008.
[30] Q. Wang and J. Wang, "Assessment Of cogging-force-reduction techniques applied to fractional-slot linear permanent magnet motors equipped with non-overlapping windings," *IET Electr. Power Appl.*, vol. 10, no. 8, pp. 697–705, Dec. 2016.
[31] F. Poltschak and P. Ebetshuber, "Design of integrated magnetic springs for linear oscillatory actuators," *IEEE Trans. Ind. Appl.*, vol. 54, no. 3, pp. 2185–2192, Jun. 2018.
[32] Q. Zhang, Y. F. Wang, and E. S. Kim, "Electromagnetic energy harvester with flexible coils and magnetic spring for 1-10 Hz resonance," *J. Microelectromech. Syst.*, vol. 24, no. 4, pp. 1193–1205, Aug. 2015.
[33] N.-B. Girtan and R. Olaru, "Improving the performance of a vibration electromagnetic actuator based on active magnetic springs," in *Proc. Int. Conf. Expo. Electr. Power Eng. (EPE)*, Iasi, Romania, Oct. 2018, pp. 284–289.
[34] Z. He, F. Dong, J. Zhao, L. Wang, J. Song, Q. Wang, and X. Song, "Thrust ripple reduction in permanent magnet synchronous linear motor based on tuned viscoelastic damper," *IEEE Trans. Ind. Electron.*, vol. 66, no. 2, pp. 98–977, Feb. 2019.
[35] B. Li, J. Zhao, X. Liu, Y. Guo, H. Hu, and J. Li, "Detent force reduction of an arc-linear permanent-magnet synchronous motor by using compensation windings," *IEEE Trans. Ind. Electron.*, vol. 64, no. 4, pp. 3001–3011, Apr. 2017.
[36] T. Shi, Y. Cao, G. Jiang, X. Li, and C. Xia, "A torque control strategy for torque ripple reduction of brushless DC motor with nonideal back electromotive force," *IEEE Trans. Ind. Electron.*, vol. 64, no. 6, pp. 4423–4433, Jun. 2017.
[37] K. K. Tan and S. Zhao, "Adaptive force ripple suppression in iron-core permanent magnet linear motors," in *Proc. IEEE Int. Symp. Intell. Control*, Vancouver, BC, Canada, Oct. 2002, pp. 266–269.
[38] M. Wang, L. Li, and D. Pan, "Detent force compensation for PMLSM systems based on structural design and control method combination," *IEEE Trans. Ind. Electron.*, vol. 62, no. 11, pp. 6845–6854, Nov. 2015.
[39] F. Ding et al, "The convergence of the forgetting factor algorithm for identifying time-varying system," *Control Theory Appl.*, vol. 11, no. 5, pp. 634–638, Oct. 1994.
[40] A. Boduroglu, Y. Demir, B. Cumhur, and M. Aydin, "A novel track structure of double-sided linear PM synchronous motor for low cost and high force density applications," *IEEE Trans. Magn.*, vol. 57, no. 2, pp. 1–5, Feb. 2021.

MEILING TANG received the master's degree in power electronics and electric drives from Sichuan University, China, in 2005, and the Ph.D. degree from the School of Electrical Engineering, Southwest Jiaotong University. She is currently an Associate Professor with Hangzhou Wanxiang Polytechnic. She has been working on power electronics and power transmission and motor control for 15 years.

YU ZOU received the B.S. degree from Hubei University, in 2010, the master's degree from the College of Mechatronics and Control Engineering from Shenzhen University, in 2013, and the Ph.D. degree from The Hong Kong Polytechnic University, in 2019.

SHENGXIAN ZHUANG received the Ph.D. degree from the University of Electronic Science and Technology of China, in 1999. From 1999 to 2003, he was a Postdoctoral Researcher at Zhejiang University and Linköping University, Sweden. He worked as a Visiting Professor with the Paderborn University of Germany, in 2005. He is currently a Professor with the School of Electrical Engineering, Southwest Jiaotong University. His research interests include energy conversion and motor drive, power electronic device&converter, and high speed VLSI signal processing.

KA WAI ERIC CHENG (Fellow, IEEE) received the B.Sc. and Ph.D. degrees from the University of Bath, in 1987 and 1990, respectively.

Before, he joined The Hong Kong Polytechnic University, in 1997. He was with Lucas Aerospace, U.K., as a Principal Engineer. He is currently a Professor and the Director of the Power Electronics Research Centre. He has published over 200 papers and seven books. He received the IEE Sebastian Z De Ferranti Premium Award, in 1995, the Outstanding Consultancy Award, in 2000, and the Faculty Merit Award for Best Teaching from the University and Silver Award of the 16th National Exhibition of Inventions, in 2003.